Shock-compressed silicon: Hugoniot and sound speed up to 2100 GPa

B. J. Henderson [1,2] M. C. Marshall,[1] T. R. Boehly,[1] R. Paul,[1,3] C. A. McCoy,[4] S. X. Hu [1] D. N. Polsin,[1,3]
L. E. Crandall [1,2] M. F. Huff,[1,2] D. A. Chin [1,2] J. J. Ruby,[1,2] X. Gong [1,3] D. E. Fratanduono,[5] J. H. Eggert,[5]
J. R. Rygg,[1,2,3] and G. W. Collins[1,2,3]

[1]*Laboratory for Laser Energetics, University of Rochester, Rochester, New York 14623-1299, USA*
[2]*Department of Physics and Astronomy, University of Rochester, Rochester, New York 14627, USA*
[3]*Department of Mechanical Engineering, University of Rochester, Rochester, New York 14627, USA*
[4]*Sandia National Laboratories, PO Box 5800, Albuquerque, New Mexico 87185-1189, USA*
[5]*Lawrence Livermore National Laboratory, Livermore, California 94550, USA*

High-pressure equation of state and isentropic sound speed data for fluid silicon to pressures of 2100 GPa (21 Mbar) are reported. Principal Hugoniot measurements were performed using impedance matching techniques with α-quartz as the reference. Sound speeds were determined by time correlating imposed shock-velocity perturbations in both the sample (Si) and reference material (α-quartz). A change in shock velocity versus particle velocity (u_s–u_p) slope on the fluid silicon principal Hugoniot is observed at 200 GPa. Density functional theory based quantum molecular dynamics simulations suggest that both an increase in ionic coordination and a 50% increase in average ionization are coincident with this experimentally observed change in slope.

I. INTRODUCTION

The behavior of silicon (Si) above millions of atmospheres (>100 GPa) is important for understanding the structure and evolution of terrestrial planets [1–4], as well as the performance of inertial confinement fusion (ICF) capsule designs [5–9]. In rocky planets, Si is thought to be intrinsically paired to oxygen and, to a lesser extent, metals since they are prevalent on Earth's surface. However, it is likely that atomic bonding and compound formation are quite different at the extreme pressures expected in super-Earth-like planets [10]. In direct-drive ICF target design, materials are selected based on a variety of properties at pressures exceeding several TPa [5]. Si has been proposed as a dopant for plastic shells [8] to mitigate laser imprint and Rayleigh–Taylor instabilities. While there has been significant work understanding the behavior of carbon [11–14] at TPa pressures, very little is understood about its group-14 analog, Si, at these extreme conditions.

Silicon has a rich and complex response to dynamic compression—in part due to strong variations in elastic properties along different crystal axes [15], which causes significant wave splitting. Elastic coefficients for silicon's cubic-diamond structure ($\rho_0 = 2.329\,\text{g/cm}^3$) determine the ambient longitudinal sound speed (c_L) along $\langle 100 \rangle$ to be 8.8 km/s and the bulk sound speed (c_B) to be 6.5 km/s. Previous experiments using explosive [16,17], flyer plate [18–20], and laser [21] drivers have been performed to investigate silicon's response to dynamic loading to 200 GPa. These works predominately used shock waves traveling at velocities below c_L (and sometimes below c_B), which form elastic and inelastic precursors, where the final shock state is a product of multiwave compression. Shocks propagating faster than $c_L(P = 80\,\text{GPa})$, the region considered for this study, do not form precursors; the silicon samples are compressed by a single wave. This present work examines the liquid regime of silicon's principal Hugoniot, extending the experimentally determined equation of state (EOS) to TPa pressures. These experiments used impedance matching [22] to an α-quartz standard, high-precision velocimetry [23], and an unsteady-waves correction [24] to deduce the kinematic properties and sound speed of shocked silicon.

Principal Hugoniot and sound-speed data are presented for silicon at shock pressures between 320 and 2100 GPa. These Hugoniot data exhibit a significantly different (u_s–u_p) slope ($S = 1.26 \pm 0.06$) from the measurements of Ref. [16] ($S = 1.80 \pm 0.10$) at lower pressures (80–200 GPa). A change in Hugoniot slope can point to a significant structural change in the material, e.g., solid-solid phase transitions or melting [25,26], dissociation [27], or ionization [28,29]. To explain the change in Hugoniot slope, quantum molecular dynamics (QMD) simulations were performed at various points along silicon's principal Hugoniot. These simulations predict an increase in ionic coordination and average ionization (average number of free electrons per atom), which is concurrent with the experimentally observed change in slope. Finally, the isentropic sound speeds c_s were determined to increase from 15 to 23 km/s at densities from 5.7 to 7.6 g/cm³, by time correlating the arrival of imposed acoustic perturbations at the shock front.

The experimental results are compared to modern theoretical calculations and tabular equations of state (*SESAME* 3810 [30], density functional theory-based first-principles EOS (DFT-based FPEOS) [31], Livermore EOS (LEOS) 141 [32,33], and XEOS 140 [34,35]). To date, the DFT-based FPEOS approach produces the best overall representation of silicon's principal Hugoniot and sound-speed data above 80 GPa.

TABLE I. Laser pulse parameters for all shots included in this dataset. Parameters include pulse duration and type [shown in Fig. 1(c)], laser spot diameter [location on target shown in Fig. 1(d)], energy delivered on the target, and the laser intensity at maximum. Data are ordered by increasing shot number. Spot diameters with an asterisk used one defocused beam with a diameter of 1.6 mm.

Shot number	Pulse type	Spot diameter (mm)	Energy on target (kJ)	Intensity at maximum (W/cm^2)
24254	5-ns square	1.1*	9.95	1.8×10^{14}
24255	5-ns square	1.1*	5.74	8.8×10^{13}
24264	5-ns square	1.1*	12.9	2.4×10^{14}
25374	5-ns square	1.1*	9.76	1.8×10^{14}
25376	5-ns square	1.1*	6.10	9.4×10^{13}
25378	5-ns square	1.1*	4.56	7.1×10^{13}
25379	5-ns square	1.1	6.91	1.5×10^{14}
25381	5-ns square	1.1*	3.11	4.9×10^{13}
25382	5-ns square	1.1	3.55	7.5×10^{13}
25384	5-ns square	1.1*	1.45	2.3×10^{13}
25385	4-ns square	1.1	6.10	1.6×10^{14}
25387	4-ns square	1.1*	11.6	2.7×10^{14}
26632	5-ns ramp top	1.8	12.0	2.5×10^{14}
26634	5-ns ramp top	1.8	5.59	1.2×10^{14}
26638	5-ns ramp top	1.8	3.85	8.1×10^{13}
26640	4-ns ramp top	1.8	7.52	2.0×10^{14}
26641	4-ns ramp top	1.8	10.5	2.8×10^{14}

II. EXPERIMENTAL TECHNIQUE

Experiments were conducted on the OMEGA EP Laser System at the University of Rochester's [36] Laboratory for Laser Energetics. Targets were irradiated by one to four 351-nm laser beams directly onto a parylene-*n* (CH) ablator, producing strong shock waves that compress the planar samples [37–41]. These experiments used laser intensities of 30–305 TW/cm^2 produced by 4- and 5-ns temporally square and ramp-top laser pulses with spot sizes of approximately 1100 or 1800 μm. Laser parameters for each shot are in Table I, and the laser pulse profiles are shown in Fig. 1(c). A portion of these experiments imposed acoustic perturbations on adjacent sides of the target stack, enabling a sound-speed determination.

The target design, shown in Fig. 1(a), comprises a 40-μm-thick CH ablator, 90-μm-thick α-quartz pusher ($\rho_{0,\text{Qz}} = 2.65$ g/cm^3, $n_0 = 1.547$ at 532 nm), 78-μm-thick silicon sample ($\rho_{0,\text{Si}} = 2.329$ g/cm^3, single crystal $\langle 100 \rangle$), 150-μm-thick α-quartz witness, and 85-μm-thick α-quartz anvil. Silicon samples were laser cut into 1.5×3-mm rectangles and oriented so the shock propagated along the $\langle 100 \rangle$ crystal axis. Crystalline silicon has a maximum oxide layer thickness of 14 Å at room temperature [42]. In these experiments the oxide layer equilibrates in under 200 fs, and therefore has a negligible effect on the measurement. Low-viscosity epoxy was used to bond the individual target components. Prior to bonding, sample thicknesses were measured with a dual confocal microscope to an accuracy of 2%; glue layers were characterized by measuring target thickness after assembly, with an average thickness and uncertainty of 3.6 and 0.4 μm, respectively.

The shock velocity in the quartz pusher, witness, and anvil were measured using a line-imaging velocity interferometer system for any reflector (VISAR) [23]. A VISAR-side image of the target is shown in Fig. 1(d) and an example of a VISAR record is shown in Fig. 1(b). The vertical position

of the fringes is proportional to shock velocity. Silicon is opaque to the 532-nm VISAR probe so the shock velocity cannot be measured within the sample. Instead, an average shock velocity is determined by a transit-time measurement using shock-breakout signatures at the bare $\sim$100-μm-wide pusher/vacuum (Si entrance) and silicon/vacuum (Si exit) interfaces. The resolution of the VISAR streak cameras enables transit-time measurements with $\sim$1–2% accuracy. Transit times in the epoxy layer preceding the Si sample are calculated from the measured thickness and inferred shock velocity, which is estimated by impedance matching [22] using *SESAME* 7603 for epoxy. This epoxy shock transit time is subtracted from the VISAR-measured transit time through the combined epoxy/silicon layer to determine the transit time through the silicon sample. A linear extrapolation of the silicon velocity profile was performed across the epoxy layer [14,43] at the pusher/silicon interface, extending the inferred silicon velocity profile backward across the epoxy, and modeling an event where the quartz and silicon are in perfect contact. The quartz witness, adjacent to the silicon sample, acts as a reference to determine the time-dependent shock velocity in the Si using the unsteady-waves correction. A quartz anvil is attached to the rear side of the silicon sample to observe acoustic perturbations after the shock exits the Si samples.

III. ANALYSIS AND RESULTS

A. Hugoniot

The principal Hugoniot data were determined by inferring shock and particle velocity using an unsteady-waves correction and impedance matching, respectively; α-quartz was used as a reference material for both techniques.

Impedance matching [22] was performed at the quartz pusher/silicon interface, where the conservation of mass, momentum, and energy was used to calculate pressure, density,
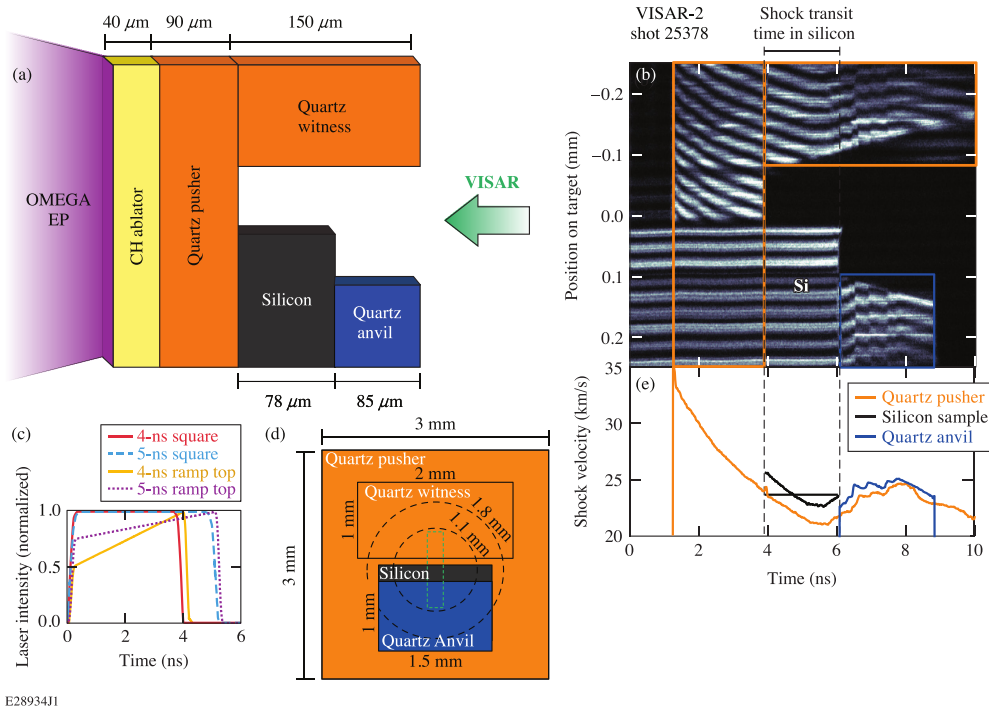
FIG. 1. (a) The target design for silicon Hugoniot measurements. Components include a CH ablator, a quartz pusher and witness, a silicon sample, and a quartz anvil. (b) VISAR record from shot 25 378 using the target depicted in (a). The *in situ* shock velocity in quartz is determined from the shifts in the fringe pattern. Silicon is opaque to the 532-nm VISAR probe laser, resulting in no fringe motion on the bottom half of the image until the shock enters the quartz anvil at 6 ns. (c) Laser intensity profiles for the four pulse shapes used in these experiments. (d) VISAR side image of the target design, showing lateral dimensions of the target components, diameters/locations of the laser spots (black dashed lines), and the VISAR field of view (green dashed lines). (e) Extracted shock velocity profiles from the VISAR record in (b). The velocity profile in silicon (black curve) was inferred from the average shock velocity (horizontal black) and the observed velocity profile in the quartz witness (orange curve) using the unsteady-waves correction. The shock-velocity history in the quartz anvil (blue curve) is observed after the shock exits the silicon sample.

and particle velocity (P, ρ, and u_p) in the shocked silicon. P, ρ, and u_p in the shocked α-quartz were calculated using an analytic fit to experimental Hugoniot data in the 0.1–1.6-TPa range [44], which was extended to 3 TPa (well above this study's highest pressures) using first-principles MD simulations [45]. A Mie–Grüneisen linear reference (MGLR) [45] model was used for the quartz release when the shock transits from higher-impedance quartz into slightly lower-impedance silicon. Since quartz and silicon have similar impedances, the resulting release produced only slightly lower pressures. Uncertainty in the impedance matching calculations were determined using a Monte Carlo routine (10^6 trials), which incorporates systematic uncertainties in the EOS, MGLR model, and random uncertainties in the measurements, yielding 1σ confidence intervals in the reported Hugoniot values.

For impedance matching with opaque materials, systematic uncertainties can arise from unsteadiness in the shock velocity within the sample. To address this, adjacent components in the target (see Fig. 1), which experience a common drive pressure profile with the sample [24], were used to infer the time-dependent velocity profile within the silicon samples and more accurately determine the shock velocity at the interface where impedance matching is performed. For these quasi-steady shock waves with small acoustic perturbations ($\Delta P/P <$ 10%), linear scaling factors (F, G) are used to determine the relative arrival times and amplitudes of perturbations at the

silicon shock front with respect to a reference medium (the α-quartz witness). Calculations of the linear scaling factors require estimates of the EOS, Grüneisen parameter, and sound speed for both quartz and silicon. The Grüneisen parameter for α-quartz is fixed at 0.66, which has been shown to be valid for shock pressures above 0.3 TPa in liquid silica [46]. The α-quartz sound speed was obtained from an empirical wide-range EOS, which was validated by experimental data in the 0.25–1.5-TPa range [47]. Estimates of the required parameters for silicon were taken from the DFT-based FPEOS from Ref. [31]. This analysis enables one to accurately infer the shock velocity profile within the sample and to determine the instantaneous shock velocity at the impedance-matching interface. Details of this technique are discussed at length in Refs. [14,46,48]. The scaling factors used for each shot are listed in Table II.

An example of the applied unsteady-waves correction can be seen in Fig. 1(e). The orange curve is the measured u_s in the quartz pusher (1.5–4 ns) and quartz witness (4–10 ns). The shock transits the silicon from about 4 to 6 ns. After 6 ns, the shock is observed in both the quartz witness and the quartz anvil (6–9 ns) on the rear of the silicon. The average u_s (horizontal black line) in the silicon is determined from the sample thickness and shock transit time (vertical black dashed lines). The measured $u_s(t)$ in the adjacent quartz witness is used to infer the velocity history in the silicon (black curve). In

TABLE II. Impedance match parameters [shock velocity in quartz (u_s^{Qz}) and silicon (u_s^{Si})], linear scaling factors (F and G) used with the average shock velocity in silicon ($\overline{u_s^{Si}}$) to infer u_s^{Si}, and Hugoniot results for silicon including particle velocity (u_p), pressure (P), and density (ρ) for all shots included in this work.

Shot number	u_s^{Qz} (km/s)	$\overline{u_s^{Si}}$ (km/s)	F	G	u_s^{Si} (km/s)	u_p (km/s)	P (GPa)	ρ (g/cm³)
26638	15.5 (0.2)	16.3 (0.2)	0.95	1.08	15.5 (0.3)	8.9 (0.2)	321 (7)	5.42 (−0.18, +0.25)
25384	16.6 (0.2)	16.8 (0.5)	0.97	1.11	17.5 (0.6)	9.5 (0.2)	389 (12)	5.12 (−0.20, +0.41)
26634	17.8 (0.2)	18.5 (0.4)	0.97	1.06	18.0 (0.5)	10.6 (0.2)	443 (11)	5.66 (−0.16, +0.48)
26640	21.5 (0.2)	23.1 (1.3)	0.95	1.03	22.0 (1.4)	13.5 (0.2)	692 (13)	6.00 (−0.13, +0.37)
25381	22.3 (0.2)	21.4 (0.6)	1.00	1.08	23.5 (0.6)	14.0 (0.2)	766 (17)	5.73 (−0.14, +0.47)
26632	23.0 (0.2)	22.7 (1.3)	1.00	1.05	22.8 (1.4)	14.8 (0.2)	788 (14)	6.63 (−0.25, +0.41)
25382	23.2 (0.2)	22.9 (0.5)	1.03	1.07	22.9 (0.6)	15.0 (0.2)	799 (18)	6.69 (−0.32, +0.60)
26641	24.0 (0.2)	25.1 (0.6)	1.00	1.01	24.2 (0.6)	15.6 (0.2)	877 (19)	6.57 (−0.37, +0.49)
25378	24.0 (0.2)	23.6 (0.9)	1.02	1.07	25.8 (0.9)	15.2 (0.3)	914 (23)	5.70 (−0.19, +0.54)
24255	23.8 (0.2)	25.6 (1.0)	0.99	1.05	26.5 (1.1)	14.9 (0.2)	921 (30)	5.32 (−0.09, +0.64)
25376	27.2 (0.2)	25.5 (0.7)	1.07	1.07	28.2 (0.7)	18.0 (0.3)	1184 (25)	6.45 (−0.33, +0.49)
25379	28.9 (0.2)	29.0 (0.7)	1.08	1.02	30.0 (0.8)	19.4 (0.3)	1353 (28)	6.60 (−0.19, +0.66)
24254	30.3 (0.2)	31.3 (0.8)	1.04	1.01	32.1 (0.9)	20.4 (0.3)	1527 (32)	6.41 (−0.23, +0.60)
25374	31.2 (0.2)	30.3 (1.1)	1.09	1.02	32.3 (1.2)	21.3 (0.3)	1604 (41)	6.87 (−0.51, +0.77)
25385	31.7 (0.2)	30.1 (0.7)	1.09	1.04	32.7 (0.8)	21.8 (0.3)	1659 (32)	7.01 (−0.22, +0.73)
24264	34.2 (0.2)	33.1 (1.2)	1.07	1.00	34.5 (1.3)	24.0 (0.3)	1918 (50)	7.65 (−0.56, +1.12)
25387	35.6 (0.2)	34.0 (1.2)	1.09	1.00	36.1 (1.3)	25.1 (0.3)	2112 (56)	7.64 (−0.48, +1.23)

this example, there is a difference of $\Delta u_s = 2.2$ km/s (about 9% of average u_s) between the average u_s and inferred initial u_s when the shock enters the silicon, with an average velocity uncertainty of 0.2 km/s. Perturbations originating from fluctuations in drive intensity (ΔI_L) are observed on the quartz witness later than in the silicon sample. To study systematic uncertainties in the inferred u_s associated with a choice of EOS in the unsteady-waves correction, two cases were tested: (1) Hugoniot parameters from *SESAME* 7387 (α-quartz) [49] and 3810 (silicon) [30], and (2) Hugoniot parameters from Ref. [45] (α-quartz) and the DFT-based FPEOS [31] (silicon). Results differed by less than their uncertainty; therefore, the empirically determined [45] and modern computational EOS [31] were used for the correction.

The Hugoniot results are listed in Table II and plotted in Fig. 2. Shock and particle velocity data from this work and four data points from Ref. [16] are fit separately using a weighted linear regression (method described in Ref. [50]). This study is restricted to the high-pressure single-wave regime, where shocked silicon does not form elastic and inelastic precursors; only Hugoniot data with pressure greater than 80 GPa are included in the fit. Linear, quadratic, and bilinear functions were compared through a general linear F-test criterion, evaluated at the 1σ probability cutoff. An additional Bayesian statistical inference method [51] was used for model selection, comparing a bilinear model against global linear and quadratic models through the Bayes factor, and testing systematic uncertainties between our work and results in Ref. [16]. According to the F-test and Bayes test, the bilinear model best represents silicon's response to shock compression for shock pressures greater than 80 GPa. Using a χ^2 minimization, the break point between the two linear regions was found at $u_{p,\text{break}} = 6.5$ km/s. Parameters of the model and their 1σ confidence intervals are in Table III; an orthogonal basis imposed on the functional form removes

correlation between the slope and intercept. For fluid velocities of $4 \leqslant u_p \leqslant 6.5$ km/s along the Hugoniot, a linear fit to Ref. [16] exhibits slope $a_1 = \Delta u_s / u_p = 1.80 \pm 0.10$, with functional form:

$$u_s = 10.3(\pm 0.1) + 1.80(\pm 0.10)(u_p - 4.95). \qquad (1)$$

Uncertainty in the velocity data of Ref. [16] is assumed to be 0.1 km/s, based on their reported significant figures. Above $u_p \geqslant 6.5$ km/s, silicon's Hugoniot "softens," and a fit to the data exhibits a shallower slope of $a_1 = 1.26 \pm 0.06$ with similar functional form:

$$u_s = 22.5(\pm 0.2) + 1.26(\pm 0.06)(u_p - 14.0). \qquad (2)$$

Residuals with respect to the bilinear fit are inset in Fig. 2(a), showing that the DFT-based FPEOS [31] best represents the experimental results for liquid silicon's Hugoniot. Figure 2(b) shows the same experimental data, fit, and models in P–ρ space. Further discussion of the Hugoniot models and discussion of the change in compressibility are included in Secs. III C and III D, respectively.

B. Isentropic sound speed

Minor perturbations imposed on the laser drive ($\Delta I_L \leqslant 5\%$) generate acoustic waves that propagate at the local isentropic sound speed c_s and are observed as perturbations in shock velocity on both sides of the target (i.e., both the witness and sample sides). Cross correlation of perturbation patterns in the α-quartz witness and anvil allows one to determine c_s along silicon's principal Hugoniot [48]. The one-dimensional hydrocode *LILAC* [52] was used to confirm (on a shot-by-shot basis) that observed modulations in the shock velocity were correlated with the laser drive, and not, for example, wave reflections interior to the target.
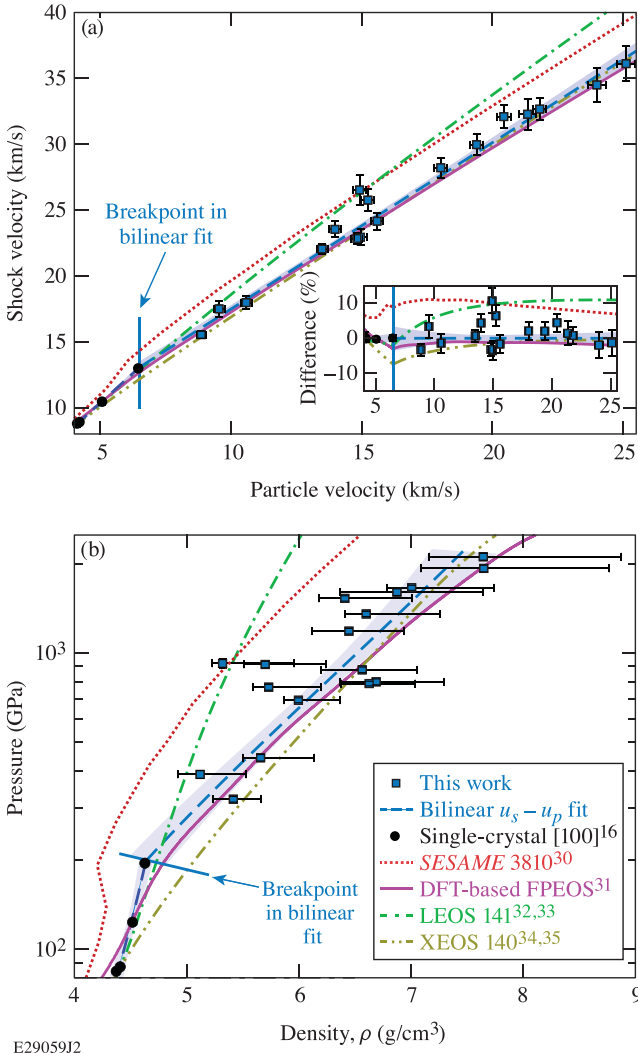
FIG. 2. Silicon principal Hugoniot in (a) shock velocity u_s versus particle velocity u_p space and (b) pressure P versus density ρ space. Only dynamic compression data above 80 GPa, the single-wave compression regime in shocked silicon, are shown. Experimental data from this work (blue squares) and Ref. [16] (black circles) are fit with a bilinear functional form (dashed blue line) with a break point at $u_p = 6.5$ km/s (solid blue line). A 1σ functional prediction band is shown as the shaded region surrounding the fit. Data are compared with Hugoniots from *SESAME* 3810 (red dotted curve), DFT-based FPEOS (pink curve), LEOS 141 (dot dash green curve), and XEOS 140 (dot dash yellow curve). Inset in (a): Percent difference in shock velocity with respect to this work's u_s–u_p fit. FPEOS shows the best agreement with the experimental Hugoniot fit and is the only model to predict the change in compressibility. The legend in (b) also corresponds to (a).

A schematic of the technique [24] used to measure sound speed is shown in Fig. 3. Using a Doppler scaling factor, F_{c_s}, perturbations observed in the quartz witness are time shifted until the arrival times match between the witness (t_{QW}) and anvil (t_{Si}). The isentropic Eulerian sound speed in silicon is then calculated from

$$c_s = \frac{P_S}{u_{p,S}\rho_S}\left(1 - \frac{(1 - M_{QW})(1 + M_{QP})}{F_{c_s}(1 - M_{QPR})}\right)^{-1}, \quad (3)$$

TABLE III. Parameters of the bilinear u_s–u_p Hugoniot fit of the form $u_s = a_0 + a_1(u_p - \beta)$ with 1σ confidence intervals. This fit is valid for shocks in silicon achieving pressures >200 GPa. Break point of the fit is $u_{p,\text{break}} = 6.5$ km/s.

Fitting range (km/s)	$a_0\,(\sigma_{a_0})$(km/s)	$a_1\,(\sigma_{a_1})$	β (km/s)
$4.0 \leqslant u_p \leqslant 6.5$ km/s	10.3 (0.09)	1.80 (0.10)	4.95
$6.5 \leqslant u_p \leqslant 25$ km/s	22.5 (0.23)	1.26 (0.06)	14.0

where P, ρ, and u_p are the pressure, density, and particle velocity, M is a local Mach number, F_{c_s} is the Doppler scaling factor ($F_{c_s} = t_{Si}/t_{QW}$), and subscripts Si, QP, QPR, and QW denote parameters of the silicon sample, quartz pusher before release, quartz pusher after release, and quartz witness, respectively [48]. Uncertainty in the sound-speed values is determined through standard error propagation using Eq. (3).

The sound-speed results are listed in Table IV and shown in Fig. 4 for all shots with observable perturbations in the quartz anvil. Results are consistent with a linear trend with increasing density. Several function forms were tested; however, due to the uncertainty in the measurements, a preferred functional form could not be determined through the general F-test criterion. Consequently, we selected a linear representation since it has the lowest number of free parameters. Experimental results from this work are fit with a simple linear model; functional form, fit parameters, and 1σ confidence intervals are listed in Table V.

C. EOS models

This work was motivated in part by a significant disagreement between models for the EOS of high-pressure silicon shocked to the fluid phase. Specifically, recent path-integral Monte Carlo (PIMC) [53] and DFT-based calculations [31,54] (FPEOS) predicted significantly higher compressibility than *SESAME* 3810 [30] and LEOS 141 [32,33]. The experiments confirmed the higher compressions predicted by FPEOS and similarly by XEOS 140 [34,35].

Below the break point, $u_p = 6.5$ km/s, corresponding to 200 GPa along the bilinear Hugoniot model, FPEOS and LEOS 141 are the most accurate representations of the silicon Hugoniot measured by Ref. [16]. Above the break point, FPEOS and XEOS 140 show the best agreement with experimental results for both the Hugoniot and sound speed in the limit of high pressures.

In fluid silicon for pressures greater than 80 GPa, the difference between the Thomas-Fermi and FPEOS models is a result of the models' treatment of atomic interaction beyond the melt ($P \approx 35$ GPa [20,21,26]). *SESAME* 3810 is a preliminary table that uses different models for solid and liquid phases, and the thermodynamic properties are smoothly interpolated (along isochores) to the ideal gas limit. Ultimately, the specific heat at constant volume is matched to the ideal gas value of $3R/2$ at high temperatures. Under such a treatment, which is implicitly monoatomic and noninteracting beyond the melt curve, clustering and/or bonding in liquids is ignored. These effects, if included, would lead to higher compressibility in physical systems. FPEOS (derived from
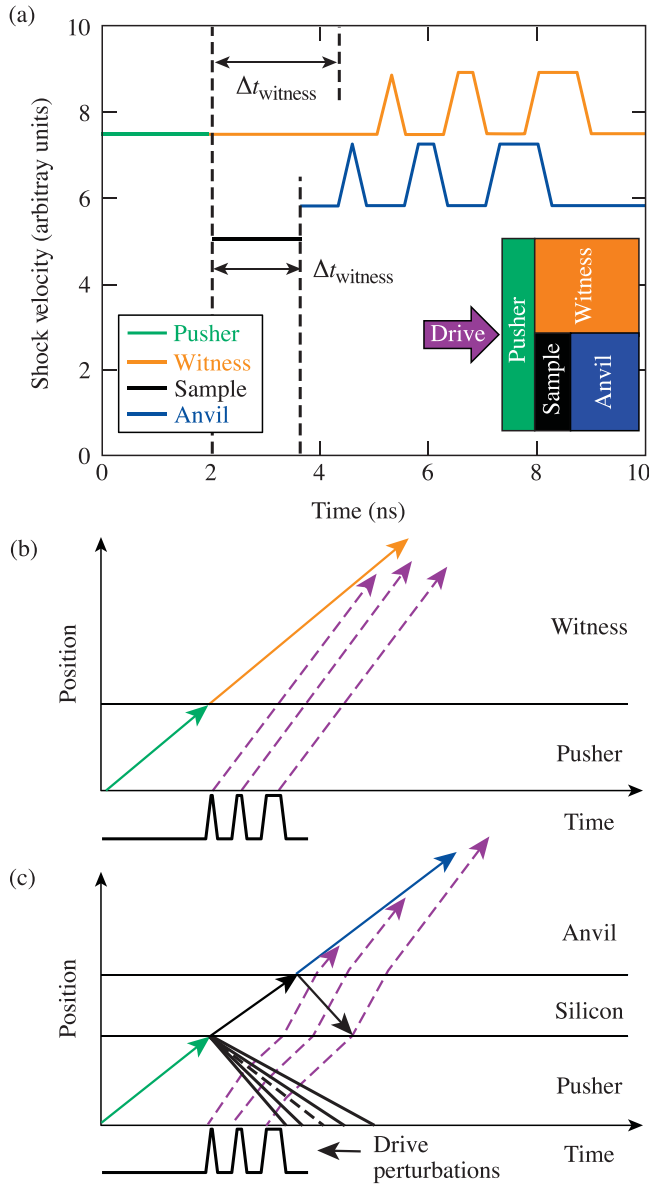
TABLE IV. Sound speed (c_s) and nonsteady waves parameter F_{c_s} included in this work.

Shot number	F_{c_s}	c_s (km/s)	ρ (g/cm^3)
25378	1.02	17.3 (1.9)	5.70 (−0.19,+0.54)
25376	1.07	18.3 (2.5)	6.45 (−0.33,+0.49)
26641	1.00	18.0 (1.7)	6.57 (−0.37,+0.49)
25379	0.95	22.3 (1.8)	6.60 (−0.19,+0.66)
25382	1.05	16.5 (2.2)	6.69 (−0.32,+0.60)
25374	1.02	22.0 (2.6)	6.87 (−0.51,+0.77)
25385	1.13	19.5 (3.7)	7.01 (−0.22,+0.73)
25387	1.05	23.2 (4.0)	7.64 (−0.48,+1.23)

a different interpolation scheme between the Debye model below melt and the ideal gas limit.

D. QMD simulations

Theoretical calculations have played an important role in explaining observed changes in physical properties of high-energy-density materials [48,55–65]. Changes in the Hugoniot slope are typically associated with ionic or electronic rearrangement. To better understand the physical mechanisms driving the change in Hugoniot slope for liquid silicon, DFT-based QMD simulations were performed to examine changes in ionic coordination under shock compression. All simulations were performed with ground state Kohn-Sham DFT [66,67] using the plane-wave implementation of DFT in the Vienna *ab initio* simulation package (VASP) [68–71], with Perdew-Burke-Ernzerhof (PBE) [72]

FIG. 3. A schematic of the technique used to determine sound speed of silicon. (a) The shock velocity is tracked in the pusher (green line), witness (orange line), and anvil (blue line). Velocity in the opaque silicon (black line) is not measured. In the witness and anvil, time and amplitude scaling factors allow us to correlate changes in velocity. Arrival times of perturbations are determined through a bilinear fit to the velocity profile near the suspected arrival. The leading shock and acoustic perturbations (dashed purple lines) are tracked in position and time on the (b) pusher/witness side and (c) pusher/silicon/anvil side. The perturbations originate from fluctuations in laser intensity at the drive surface.

DFT calculations) models these effects by using Kohn-Sham equations to solve for the mean-field approximated electron density, which, together with ion-ion interaction, drives the nuclear motion within the Born-Oppenheimer approximation. Similarly, the LEOS and XEOS tables, a quotidian EOS, rely on the Cowan model for the ionic free-energy part, an average-atom model for the electronic free energy, and are built using

FIG. 4. Isentropic sound speed along the silicon Hugoniot. Results from this work (blue squares) and a single measurement from Ref. [16] (black circle) are compared against *SESAME* 3810, DFT-based FPEOS, LEOS 141 and XEOS 140. The ambient bulk (c_B) and longitudinal (c_L along $\langle 100 \rangle$) sound speeds are indicated by the horizontal black lines. A linear model (blue line) is fit to the data and extrapolated (blue dashed line) to the left- and right-most error bar. The shaded region around the fit is the 1σ confidence interval.

TABLE V. Parameters of the linear c_s-ρ fit with 1-σ confidence intervals and correlation matrix elements. This fit is valid for shocks in silicon achieving pressures >80 GPa.

Function form	Fit parameter results	Covariance matrix	
$c_s = \beta\rho + \alpha$	$\alpha = 5.56(0.98)\,\text{km/s}$	0.96	
	$\beta = -18.5(6.65)\frac{\text{km cc}}{\text{g s}}$	-6.5	44.2

generalized gradient approximation [73] exchange-correlation functionals. Quantum molecular dynamics simulations were performed with VASP using 256-atom supercells with periodic boundary conditions. The reciprocal space was sampled using $2 \times 2 \times 2$ Monkhorst-Pack [74] **k** meshes. The ionic time-step size was 0.5 fs over 10 000 steps, yielding a total atomistic simulation time of 5 ps. Projector-augmented wave pseudopotentials [75,76] with a 1.10-Å cutoff of core radius was used with the semicore $2s^2 2p^6 3s^2 3p^2$ electrons being treated as valence electrons, corresponding to a kinetic energy cutoff of 1100 eV for the plane-wave basis set. Previous studies [77,78] have tested the applicability of the pseudopotential for shock Hugoniot conditions. At 1 TPa, the Si-Si distance is >1.5 Å, so we do not expect a density bias due to the selected pseudopotential. Electrons were populated according to

FIG. 5. Results of DFT-based MD simulations along silicon's principal Hugoniot. (a) Experimental Hugoniot results, bilinear u_s–u_p fit, and the DFT-based FPEOS. The break point in the fit (vertical blue line) is located at $\rho = 4.64\,\text{g/cm}^3$, or $P = 200$ GPa along the Hugoniot fit. (b) Coordination number n and (c) average free electrons per atom $\bar{Z}$ calculated at several densities along the principal Hugoniot. Inset: Image of the liquid silicon structure from MD with coordination number 13 at ~ 1 TPa. The observed change in slope along the Hugoniot occurs at the center of a predicted rise in coordination number and the beginning of a rise in average ionization.

Fermi-Dirac statistics and all-electronic, self-consistent field calculations were converged to a precision of 10^{-5} eV/atom for the free energies.
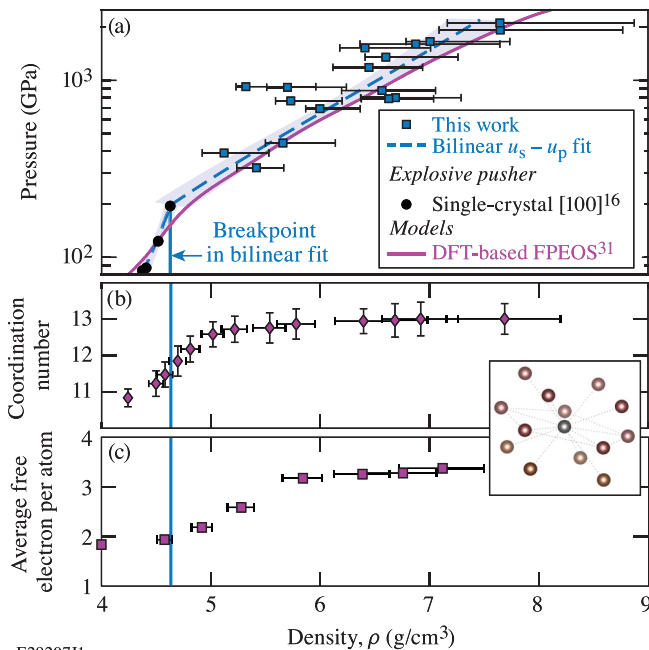
Results of the DFT-based QMD simulations of fluid silicon are shown in Fig. 5. The coordination number increases from $n \approx 11$ to $n \approx 13$ between 50 and 300 GPa [Fig. 5(b)], with the sharpest rise located near 200 GPa. Since silicon is a liquid at these pressures, the coordination numbers are calculated by approximating an isotropic crystal structure and are not constrained to a maximum coordination number of 12. The observed change in Hugoniot slope at $P = 200$ GPa, indicated by the vertical blue line at $\rho = 4.64\,\text{g/cm}^3$ in Fig. 5(a), is near the center of this rise. Previous work on structural evolution in compressed liquids has shown that silicon and tin form highly coordinated liquid structures. Static experiments on liquid silicon revealed a gradual increase in coordination with increasing pressure, measuring coordination numbers as high as 9.2 at 23 GPa [79]. In tin, another group-14 element, a coordination number of $n = 11$ was measured just above the melt on the Hugoniot (40–70 GPa), increasing to $n > 12$ around 90 GPa [80]. In silicon, $n = 11$ at 50 GPa would indicate that silicon has an isotropic fluid structure [81] just after shocking through the melt ($P = 35$ GPa). An increase to $n \approx 13$, and subsequent plateau, suggests that silicon forms a more highly coordinated isotropic fluid by 300 GPa with no further changes in ionic arrangement to 2100 GPa.

The change in Hugoniot slope is also coincident with a predicted 50% increase in the average number of free electrons per atom, due to an ionization event. Dynamic compression experiments on helium [28] and various metals [29] have made it possible to observe changes in Hugoniot slope at pressures above several hundred GPa, attributed to ionization. Figure 5(c) shows an increase in the average number of free electrons per atom, from $\bar{Z} \approx 2$ to $\bar{Z} \approx 3$, starting at 200 GPa along the fluid silicon Hugoniot. These simulations suggest that above 500 GPa, and up to 1200 GPa, $\bar{Z}$ is nearly constant.

IV. CONCLUSIONS

The behavior of nature's fundamental building blocks at millions of atmospheres is important in studies of astrophysical bodies [1–4] and ICF capsule designs [5–9]. *In situ* observation of these materials deep in the interior of planets and stars is technologically infeasible, necessitating the generation of extreme pressures and temperatures in the laboratory. With little intuition for the bonding or compounds that might form at such extreme conditions, these macroscopic thermodynamic studies provide rigorous benchmarks for theory and first principles simulations, through which we can gain insight into the microscopic behavior.

Reported here are shock-compressed measurements of silicon, along the principal Hugoniot, to a high-pressure liquid phase in the range of 320–2100 GPa, and achieving a maximum of 3.3-fold compression. Combined with existing data from Ref. [16], the experimental results are well represented by a bilinear fit determined by a weighted least-squares fitting over an orthogonal basis. A change in Hugoniot slope is detected near $P = 200$ GPa, and simulations were performed to examine the underlying physical processes. DFT-based QMD

simulations suggest that the experimentally observed change in Hugoniot slope is coincident with an increase in ionic coordination and average ionization. By correlating acoustic perturbations on both sides of the target, the sound speed was determined to be $15 < c_E(\text{km/s}) < 23$ at $800 < P(\text{GPa}) < 2100$ and $5.7 < \rho(\text{g/cm}^3) < 7.6$ along the Hugoniot. Of the best available theoretical calculations, A DFT-based FPEOS [31] table shows the most overall agreement with experimental results.

[1] E. J. Davies, P. J. Carter, S. Root, R. G. Kraus, D. K. Spaulding, S. T. Stewart, and S. B. Jacobsen, Silicate melting and vaporization during rocky planet formation, J. Geophys. Res. Planets **125**, e2019JE006227 (2020).

[2] J. E. Chambers, Making more terrestrial planets, Icarus **152**, 205 (2001).

[3] A. Benuzzi-Mounaix, S. Mazevet, R. Ravasio, T. Vinci, A. Denoeud, M. Koenig, N. Amadou, E. Brambrink, F. Festa, A. Levy *et al.*, Progress in warm dense matter study with applications to planetology, Phys. Scr. **2014**, 014060 (2014).

[4] Y. Zhang, T. Sekine, H. He, Y. Yu, F. Liu, and M. Zhang, Shock compression of Fe-Ni-Si system to 280 GPa: Implications for the composition of the earth's outer core, Geophys. Res. Lett. **41**, 4554 (2014).

[5] R. S. Craxton, K. S. Anderson, T. R. Boehly, V. N. Goncharov, D. R. Harding, J. P. Knauer, R. L. McCrory, P. W. McKenty, D. D. Meyerhofer, J. F. Myatt *et al.*, Direct-drive inertial confinement fusion: A review, Phys. Plasmas **22**, 110501 (2015).

[6] V. N. Goncharov, T. C. Sangster, R. Betti, T. R. Boehly, M. J. Bonino, T. J. B. Collins, R. S. Craxton, J. A. Delettrez, D. H. Edgell, R. Epstein *et al.*, Improving the hot-spot pressure and demonstrating ignition hydrodynamic equivalence in cryogenic deuterium–tritium implosions on OMEGA, Phys. Plasmas **21**, 056315 (2014).

[7] G. Fiksel, S. X. Hu, V. N. Goncharov, D. D. Meyerhofer, T. C. Sangster, V. A. Smalyuk, B. Yaakobi, M. J. Bonino, and R. Jungquist, Experimental reduction of laser imprinting and Rayleigh–Taylor growth in spherically compressed, medium-Z-doped plastic targets, Phys. Plasmas **19**, 062704 (2012).

[8] S. X. Hu, G. Fiksel, V. N. Goncharov, S. Skupsky, D. D. Meyerhofer, and V. A. Smalyuk, Mitigating Laser Imprint in Direct-Drive Inertial Confinement Fusion Implosions with High-Z dopants, Phys. Rev. Lett. **108**, 195003 (2012).

[9] G. Huser, N. Ozaki, P. Colin-Lalu, V. Recoules, T. Sano, Y. Sakawa, K. Miyanishi, and R. Kodama, Hugoniot equation of state of Si-doped glow discharge polymer and scaling to other plastic ablators, Phys. Plasmas **25**, 052706 (2018).

[10] H. Niu, A. R. Oganov, X.-Q. Chen, and D. Li, Prediction of novel stable compounds in the Mg-Si-O system under exoplanet pressures, Sci. Rep. **5**, 18347 (2015).

[11] R. F. Smith, J. H. Eggert, R. Jeanloz, T. S. Duffy, D. G. Braun, J. R. Patterson, R. E. Rudd, J. Biener, A. E. Lazicki, A. V. Hamza *et al.*, Ramp compression of diamond to five terapascals, Nature (London) **511**, 330 (2014).

[12] D. G. Hicks, T. R. Boehly, P. M. Celliers, D. K. Bradley, J. H. Eggert, R. S. McWilliams, R. Jeanloz, and G. W. Collins, High-precision measurements of the diamond Hugoniot in and above the melt region, Phys. Rev. B **78**, 174102 (2008).

[13] D. K. Bradley, J. H. Eggert, D. G. Hicks, P. M. Celliers, S. J. Moon, R. C. Cauble, and G. W. Collins, Shock Compressing Diamond to a Conducting Fluid, Phys. Rev. Lett. **93**, 195506 (2004).

[14] M. C. Gregor, D. E. Fratanduono, C. A. McCoy, D. N. Polsin, A. Sorce, J. R. Rygg, G. W. Collins, T. Braun, P. M. Celliers, J. H. Eggert *et al.*, Hugoniot and release measurements in diamond shocked up to 25 Mbar, Phys. Rev. B **95**, 144114 (2017).

[15] M. A. Hopcroft, W. D. Nix, and T. W. Kenny, What is the Young's modulus of silicon? J. Microelectromech. S. **19**, 229 (2010).

[16] M. N. Pavlovskii, Formation of metallic modifications of germanium and silicon under shock loading, Sov. Phys. Solid State **9**, 2514 (1968).

[17] W. H. Gust and E. B. Royce, Axial yield strengths and two successive phase transition stresses for crystalline silicon, J. Appl. Phys. **42**, 1897 (1971).

[18] T. Goto, T. Sato, and Y. Syono, Reduction of shear strength and phase-transition in shock-loaded silicon, Jpn. J. Appl. Phys. **21**, L369 (1982).

[19] S. Turneaure and Y. M. Gupta, Inelastic deformation and phase transformation of shock compressed silicon single crystals, Appl. Phys. Lett. **91**, 201913 (2007).

[20] S. J. Turneaure, S. M. Sharma, and Y. M. Gupta, Nanosecond Melting and Recrystallization in Shock-Compressed Silicon, Phys. Rev. Lett. **121**, 135701 (2018).

[21] E. E. McBride, A. Krygier, A. Ehnes, E. Galtier, M. Harmand, Z. Konôpková, H. J. Lee, H. P. Liermann, B. Nagler, A. Pelka *et al.*, Phase transition lowering in dynamically compressed silicon, Nat. Phys. **15**, 89 (2019).

[22] Ya. B. Zel'dovich and Yu. P. Raĭzer, in *Physics of Shock Waves and High-Temperature Hydrodynamic Phenomena*, edited by W. D. Hayes and R. F. Probstein (Academic, New York, 1966).

[23] P. M. Celliers, D. K. Bradley, G. W. Collins, D. G. Hicks, T. R. Boehly, and W. J. Armstrong, Rev. Sci. Instrum. **75**, 4916 (2004).

[24] D. E. Fratanduono, D. H. Munro, P. M. Celliers, and G. W. Collins, Hugoniot experiments with unsteady waves, J. Appl. Phys. **116**, 033517 (2014).

[25] O. Strickson and E. Artacho, *Ab initio* calculation of the shock Hugoniot of bulk silicon, Phys. Rev. B **93**, 094107 (2016).

[26] R. Paul, S. X. Hu, and V. V. Karasiev, Anharmonic and Anomalous Trends in the High-Pressure Phase Diagram of Silicon, Phys. Rev. Lett. **122**, 125701 (2019).

[27] W. J. Nellis, H. B. Radousky, D. C. Hamilton, A. C. Mitchell, N. C. Holmes, K. B. Christianson, and M. van Thiel, Equation-of-state, shock-temperature, and electrical-conductivity data of dense fluid nitrogen in the region of the dissociative phase transition, J. Chem. Phys. **94**, 2244 (1991).

[28] J. Eggert, S. Brygoo, P. Loubeyre, R. S. McWilliams, P. M. Celliers, D. G. Hicks, T. R. Boehly, R. Jeanloz, and G. W. Collins, Hugoniot Data for Helium in the Ionization Regime, Phys. Rev. Lett. **100**, 124503 (2008).

[29] R. F. Trunin, Shock compressibility of condensed materials in strong shock waves generated by underground nuclear explosions, Phys. Usp. **37**, 1123 (1994).

[30] G. I. Kerley, An Equation of State for Silicon, Report No. KPS96-8, Kerley Publishing Services, Albuquerque, NM, September 1996.

[31] S. X. Hu, R. Gao, Y. Ding, L. A. Collins, and J. D. Kress, First-principles equation-of-state table of silicon and its effect on high-energy-density plasma simulations, Phys. Rev. E **95**, 043210 (2017).

[32] D. A. Young and E. M. Corey, A new global equation of state model for hot, dense matter, J. Appl. Phys. **78**, 3748 (1995).

[33] R. M. More, K. H. Warren, D. A. Young, and G. B. Zimmerman, A new quotidian equation of state (QEOS) for hot dense matter, Phys. Fluids **31**, 3059 (1988).

[34] B. Wilson, V. Sonnad, P. Sterne, and W. Isaacs, PURGATORIO—A new implementation of the INFERNO algorithm, J. Quant. Spectrosc. Radiat. Transf. **99**, 658 (2006).

[35] P. A. Sterne, S. B. Hansen, B. G. Wilson, and W. A. Isaacs, Equation of state, occupation probabilities and conductivities in the average atom Purgatorio code, High Energy Density Phys. **3**, 278 (2007).

[36] D. D. Meyerhofer, J. Bromage, C. Dorrer, J. H. Kelly, B. E. Kruschwitz, S. J. Loucks, R. L. McCrory, S. F. B. Morse, J. F. Myatt, P. M. Nilson *et al.*, Performance of and initial results from the OMEGA EP laser system, J. Phys.: Conf. Ser. **244**, 032010 (2010).

[37] S. I. Anisimov, A. M. Prokhorov, and V. E. Fortov, Application of high-power lasers to study matter at ultrahigh pressures, Sov. Phys. Usp. **27**, 181 (1984).

[38] S. A. Abrosimov, A. P. Bazhulin, V. V. Voronov, A. A. Geras'kin, I. K. Krasyuk, P. P. Pashinin, A. Yu. Semenov, I. A. Stuchebryukhov, K. V. Khishchenko, and V. E. Fortov, Specific features of behavior of targets under negative pressures created by a picosecond laser pulse, Quantum Electron. **43**, 246 (2013).

[39] I. K. Krasyuk, P. P. Pashinin, A. Yu. Semenov, K. V. Khishchenko, and V. E. Fortov, Study of extreme states of matter at high energy densities and high strain rates with powerful lasers, Laser Phys. **26**, 094001 (2016).

[40] G. W. Collins, L. B. Da Silva, P. Celliers, D. M. Gold, M. E. Foord, R. J. Wallace, A. Ng, S. V. Weber, K. S. Budil, and R. Cauble, Measurements of the equation of state of deuterium at the fluid insulator-metal transition, Science **281**, 1178 (1998).

[41] R. Cauble, T. S. Perry, D. R. Bach, K. S. Budil, B. A. Hammel, G. W. Collins, D. M. Gold, J. Dunn, P. Celliers, L. B. Da Silva *et al.*, Absolute Equation-of-State Data in the 10–40 Mbar (1–4 TPa) Regime, Phys. Rev. Lett. **80**, 1248 (1998).

[42] E. A. Taft, Growth of Native Oxide on Silicon, J. Electrochem. Soc. **135**, 1022 (1988).

[43] A. Lazicki, R. A. London, F. Coppari, D. Erskine, H. D. Whitley, K. J. Caspersen, D. E. Fratanduono, M. A. Morales, P. M. Celliers, J. H. Eggert *et al.*, Shock equation of state of 6LiH to 1.1 TPa, Phys. Rev. B **96**, 134101 (2017).

[44] M. D. Knudson and M. P. Desjarlais, Shock Compression of Quartz to 1.6 TPa: Redefining a Pressure Standard, Phys. Rev. Lett. **103**, 225501 (2009).

[45] M. P. Desjarlais, M. D. Knudson, and K. R. Cochrane, Extension of the Hugoniot and analytical release model of α-quartz to 0.2–3 TPa, J. Appl. Phys. **122**, 035903 (2017).

[46] C. A. McCoy, M. C. Gregor, D. N. Polsin, D. E. Fratanduono, P. M. Celliers, T. R. Boehly, and D. D. Meyerhofer, Measurements of the sound velocity of shock-compressed liquid silica to 1100 GPa, J. Appl. Phys. **120**, 235901 (2016).

[47] M. Li, S. Zhang, H. Zhang, G. Zhang, F. Wang, J. Zhao, C. Sun, and R. Jeanloz, Continuous Sound Velocity Measurements along the Shock Hugoniot Curve of Quartz, Phys. Rev. Lett. **120**, 215703 (2018).

[48] D. E. Fratanduono, P. M. Celliers, D. G. Braun, P. A. Sterne, S. Hamel, A. Shamp, E. Zurek, K. J. Wu, A. E. Lazicki, M. Millot *et al.*, Equation of state, adiabatic sound speed, and Grüneisen coefficient of boron carbide along the principal Hugoniot to 700 GPa, Phys. Rev. B **94**, 184107 (2016).

[49] S. Crockett, Equation-of-state tabular data for the thermodynamic properties of materials, SESAME Database, Theoretical Division, Accessed 8 May 2020, https://www.lanl.gov/org/ddste/aldsc/theoretical/physics-chemistry-materials/sesame-database.php.

[50] P. M. Celliers, G. W. Collins, D. G. Hicks, and J. H. Eggert, Systematic uncertainties in shock-wave impedance-match analysis and the high-pressure equation of state of Al, J. Appl. Phys. **98**, 113529 (2005).

[51] J. J. Ruby, J. R. Rygg, D. A. Chin, J. A. Gaffney, P. J. Adrian, D. Bishel, C. J. Forrest, V. Yu. Glebov, N. V. Kabadi, P. M. Nilson *et al.*, Constraining physical models at gigabar pressures, Phys. Rev. E **102**, 053210 (2020).

[52] J. Delettrez and E. B. Goldman, Numerical modeling of suprathermal electron transport in laser-produced plasmas, LLE Report No. 36, Laboratory for Laser Energetics, University of Rochester, Rochester, NY, 1976.

[53] B. Militzer and K. P. Driver, Development of Path Integral Monte Carlo Simulations with Localized Nodal Surfaces for Second-Row Elements, Phys. Rev. Lett. **115**, 176403 (2015).

[54] S. X. Hu, B. Militzer, L. A. Collins, K. P. Driver, and J. D. Kress, First-principles prediction of the softening of the silicon shock Hugoniot curve, Phys. Rev. B **94**, 094109 (2016).

[55] B. Boates, S. Hamel, E. Schwegler, and S. A. Bonev, Structural and optical properties of liquid CO_2 for pressures up to 1 TPa, J. Chem. Phys. **134**, 064504 (2011).

[56] J. Zhang, J. Zhu, N. Velisavljevic, L. Wang, and Y. Zhao, Thermal equation of state and thermodynamic Grüneisen parameter of beryllium metal, J. Appl. Phys. **114**, 173509 (2013).

[57] Y. Zhang, C. Wang, D. Li, and P. Zhang, Quantum molecular dynamic simulations of warm dense carbon monoxide, J. Chem. Phys. **135**, 064501 (2011).

[58] Y. Zhang, C. Wang, and P. Zhang, The electronic and optical properties of warm dense nitrous oxide using quantum molecular dynamics simulations, Phys. Plasmas **19**, 112701 (2012).

[59] S. Root, K. R. Cochrane, J. H. Carpenter, and T. R. Mattsson, Carbon dioxide shock and reshock equation of state data to 8 Mbar: Experiments and simulations, Phys. Rev. B **87**, 224102 (2013).

[60] R. J. Magyar, S. Root, and T. R. Mattsson, Equations of state for mixtures: Results from density-functional (DFT) simulations compared to high accuracy validation experiments on Z, J. Phys.: Conf. Ser. **500**, 162004 (2014).

[61] T. R. Mattsson, S. Root, A. E. Mattsson, L. Shulenburger, R. J. Magyar, and D. G. Flicker, Validating density-functional theory simulations at high energy-density conditions with liquid krypton shock experiments to 850 GPa on Sandia's Z machine, Phys. Rev. B **90**, 184105 (2014).

[62] D. Li, P. Zhang, and J. Yan, Quantum molecular dynamics simulations of the thermophysical properties of shocked liquid ammonia for pressures up to 1.3 TPa, J. Chem. Phys. **139**, 134505 (2013).

[63] M. A. Kadatskiy and K. V. Khishchenko, Comparison of Hugoniots calculated for aluminum in the framework of three quantum-statistical models, J. Phys.: Conf. Ser. **653**, 012079 (2015).

[64] M. A. Kadatskiy and K. V. Khishchenko, Theoretical investigation of the shock compressibility of copper in the average-atom approximation, Phys. Plasmas **25**, 112701 (2018).

[65] N. Yu. Orlov, M. A. Kadatskiy, O. B. Denisov, and K. V. Khishchenko, Application of quantum-statistical methods to studies of thermodynamic and radiative processes in hot dense plasmas, Matter Radiat. Extremes **4**, 054403 (2019).

[66] P. Hohenberg and W. Kohn, Inhomogeneous electron gas, Phys. Rev. **136**, B864 (1964).

[67] W. Kohn and L. J. Sham, Self-consistent equations including exchange and correlation effects, Phys. Rev. **140**, A1133 (1965).

[68] G. Kresse and J. Hafner, *Ab Initio* molecular dynamics for liquid metals, Phys. Rev. B **47**, 558 (1993).

[69] G. Kresse and J. Hafner, *Ab Initio* molecular-dynamics simulation of the liquid-metal–amorphous-semiconductor transition in germanium, Phys. Rev. B **49**, 14251 (1994).

[70] G. Kresse and J. Furthmüller, Efficiency of *ab-initio* total energy calculations for metals and semiconductors using a plane-wave basis set, Comput. Mater. Sci. **6**, 15 (1996).

[71] G. Kresse and J. Furthmüller, Efficient iterative schemes for *ab initio* total-energy calculations using a plane-wave basis set, Phys. Rev. B **54**, 11169 (1996).

[72] J. P. Perdew, K. Burke, and M. Ernzerhof, Generalized Gradient Approximation made Simple, Phys. Rev. Lett. **77**, 3865 (1996); **78**, 1396 (1997).

[73] J. P. Perdew, J. A. Chevary, S. H. Vosko, K. A. Jackson, M. R. Pederson, D. J. Singh, and C. Fiolhais, Atoms, molecules, solids, and surfaces: Applications of the generalized gradient approximation for exchange and correlation, Phys. Rev. B **46**, 6671 (1992); Erratum: **48**, 4978 (1993).

[74] H. J. Monkhorst and J. D. Pack, Special points for Brillouin-zone integrations, Phys. Rev. B **13**, 5188 (1976).

[75] P. E. Blöchl, Projector augmented-wave method, Phys. Rev. B **50**, 17953 (1994).

[76] G. Kresse and D. Joubert, From ultrasoft pseudopotentials to the projector augmented-wave method, Phys. Rev. B **59**, 1758 (1999).

[77] P. R. Levashov, G. V. Sin'ko, N. A. Smirnov, D. V. Minakov, O. P. Shemyakin, and K. V. Khishchenko, Pseudopotential and full-electron DFT calculations of thermodynamic properties of electrons in metals and semiempirical equations of state, J. Phys.: Condens. Matter **22**, 505501 (2010).

[78] G. V. Sin'ko, N. A. Smirnov, A. A. Ovechkin, P. R. Levashov, and K. V. Khishchenko, Thermodynamic functions of the heated electron subsystem in the field of cold nuclei, High Energy Density Phys. **9**, 309 (2013).

[79] N. Funamori and K. Tsuji, Pressure-Induced Structural Change of Liquid Silicon, Phys. Rev. Lett. **88**, 255508 (2002).

[80] R. Briggs, M. G. Gorman, S. Zhang, D. McGonegle, A. L. Coleman, F. Coppari, M. A. Morales-Silva, R. F. Smith, J. K. Wicks, C. A. Bolme *et al.*, Coordination changes in liquid tin under shock compression determined using *in situ* femtosecond x-ray diffraction, Appl. Phys. Lett. **115**, 264101 (2019).

[81] Y. Waseda, The structure of liquids, amorphous solids and solid fast ion conductors, Prog. Mater. Sci. **26**, 1 (1981).